Source Parameter Analysis Using Maximum Amplitudes in the Time Domain

Trey C. Knudson*[1], William L. Ellsworth[1], and Gregory C. Beroza[1]

ABSTRACT

We measure maximum amplitudes in the time domain on recordings of the 2019 Ridgecrest earthquake sequence to convert ground-motion amplitudes to source spectra. To do this, we modify Richter's local magnitude relation to measure frequency-dependent empirical amplitude-decay curves and station corrections for a series of narrowband time-domain filters. Peak displacement amplitude in each frequency band is used to construct the displacement spectrum. After correction for attenuation, we determine corner frequency and moment from the resulting source spectra. By this approach, we measure moment magnitudes reliably to as small as M_L 1.0. We find stress drop increases with both depth and magnitude and discuss whether this could be an artifact through assumptions about the source, path, and site.

KEY POINTS

- We measure seismic moment and corner frequency in the Ridgecrest sequence using time-domain peak amplitudes.
- Moment magnitudes for events as low as M_L 1.0 are reliable determined using 1/2 octave measurement filters.
- Stress drop increases with both depth and magnitude, but we cannot rule out constant stress-drop scaling.

Supplemental Material

INTRODUCTION

Measurement of seismic source properties has long been done in the frequency domain through Fourier analysis (Thatcher and Hanks, 1973). Accurate portrayal of the seismic source spectrum is important because it can be used to infer physical quantities, such as the rupture area, slip, and seismic moment via the long-period level and corner frequency. To isolate source properties, however, we need to separate them from path and site effects that are convolved with the source to form the observed spectrum,

$$d_{ij}(f) = e_i(f)st_j(f)t_{ij}(f), \tag{1}$$

in which d_{ij} is the displacement spectrum for an earthquake i at station j, e_i is the source term, st_j is the site term, and t_{ij} is a path-dependent term. Accounting for these terms is a subtle process that requires assumptions, such as removing path effects and interpreting spectra with simple models that may not fully capture the true complexity of the system (Abercrombie, 2021). Empirical Green's function (EGF) approaches have been used to help remove similar path and site effects for nearby events using fewer assumptions, but sparse catalogs, frequency-dependent signal-to-noise ratio (SNR), and other data constraints can impact the scalability of such approaches (Abercrombie *et al.*, 2021).

In this article, we employ a method developed by Al-Ismail *et al.* (2023) that extends Richter's magnitude relation (Richter, 1935) to solve for frequency-dependent propagation effects. Richter's magnitude relation is given by

$$M_L = \log_{10}(A) - \log_{10}(A_0), \tag{2}$$

in which M_L is defined as the local magnitude, A is the maximum displacement measured at a given station from a Wood–Anderson Seismograph, and A_0 is a distance correction. Despite regional variability in crustal structure and focal depth differences, the path averaged $\log_{10}(A_0)$ terms do a remarkable job of standardizing the earthquake magnitude scale to characterize earthquake size and are still widely used nearly 90 yr after they were introduced.

Time-domain measurement of maximum amplitude has previously been used to construct the seismic spectrum. Tsujiura (1973), Rautian and Khalturin (1978), Rautian *et al.* (1978), Chouet *et al.* (1978), and Aki and Chouet (1975) all used analog instruments with multiple band-pass filters to record the seismogram and measure the spectrum by reading amplitudes on the filtered waveforms.

These methods inspired us to extend the work of Al-Ismail *et al.* (2023) to measure the spectrum in the time domain from

1. Department of Geophysics, Stanford University, Stanford, California, U.S.A., https://orcid.org/0009-0007-0350-5732 (TCK); https://orcid.org/0000-0001-8378-4979 (WLE); https://orcid.org/0000-0002-8667-1838 (GCB)

*Corresponding author: trey05@stanford.edu

Cite this article as Knudson, T. C., W. L. Ellsworth, and G. C. Beroza (2025). Source Parameter Analysis Using Maximum Amplitudes in the Time Domain, *Bull. Seismol. Soc. Am.* **115**, 839–849, doi: 10.1785/0120240198

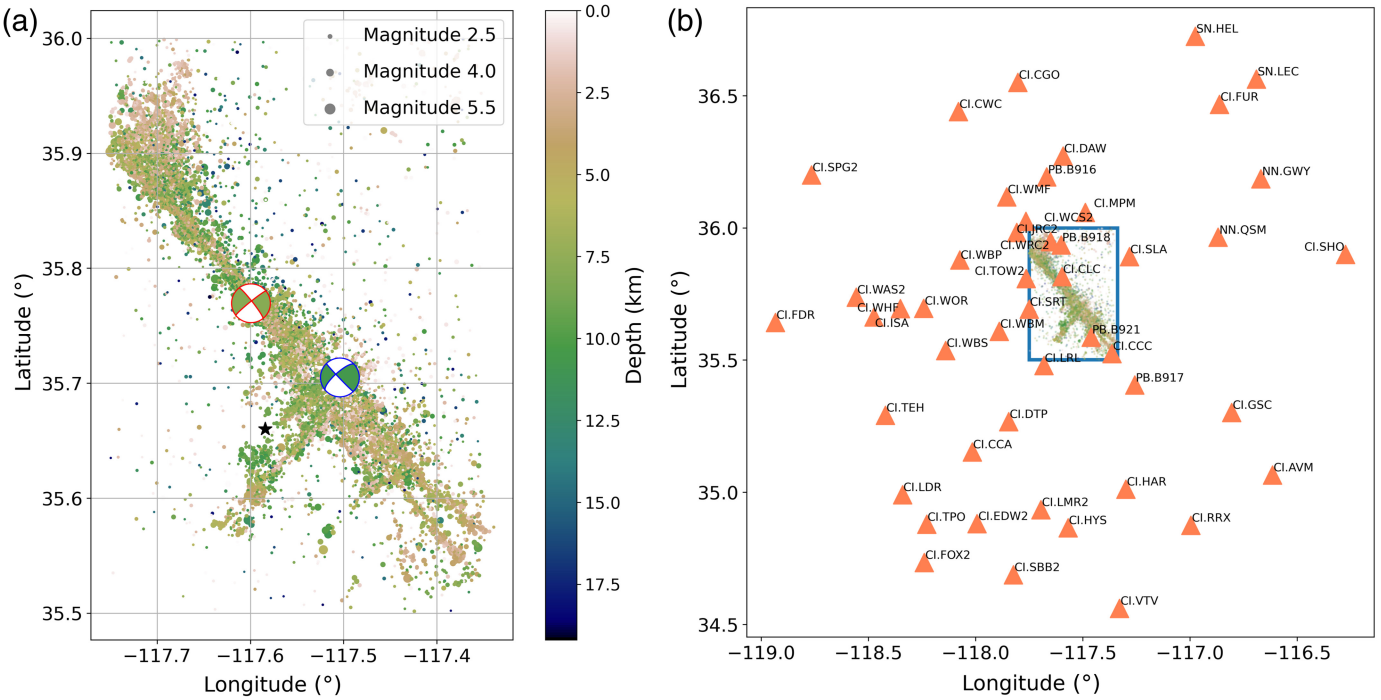

Figure 1. (a) Relocated event locations for the two weeks (4–17 July 2019) of data in the 2019 Ridgecrest sequence (Trugman, 2020). The red-outlined focal mechanism shows the event location of the right-lateral M_w 7.1 mainshock on 6 July 2019. The blue-outlined focal mechanism shows the event location of the left-lateral M_w 6.4 foreshock on 4 July 2019. The black star indicates the event location of event "38476711," M_w 3.18. (b) Locations of the 41 stations used in this study. The blue box highlights the event region shown in panel (a). The color version of this figure is available only in the electronic edition.

maximum amplitudes of digitally band-pass-filtered displacement seismograms. The amplitudes we measure are input to a workflow to solve for the path and site terms that correct for propagation effects to reveal the source spectrum. For this study, we use the data set from the two-week (4–17 July 2019) Ridgecrest catalog provided by the Southern California Earthquake Data Center (SCEDC) as part of the Southern California Earthquake Center/U.S. Geological Survey Community Stress-Drop Validation Study (Abercrombie *et al.*, 2024). The data set consists of nearly 13,000 relocated events ($M \geq 1.0$) containing auto-picked phase arrivals (Fig. 1) (Southern California Earthquake Center [SCEC], 2013). Here, we analyze the 41 stations shown in Figure 1 from the Southern California Seismic Network (CI), Plate Boundary Observatory Borehole seismic network (PB), and Nevada Seismic Network (NN).

The data set encompasses both the M_w 6.4 foreshock from 4 July 2019 and the M_w 7.1 mainshock that occurred ~34 hr later on 6 July 2019. These two earthquakes and their aftershocks illuminate complex cross-fault ruptures that occurred along a series of subfaults rather than clearly defined planar faults (Barnhart *et al.*, 2019; Ross *et al.*, 2019; Shelly, 2020). Specifically, the center of the sequence contains a series of interlocking orthogonal fault structures that suggest a less developed fault zone than the northwest section, which exhibits slightly more uniformity (Ross *et al.*, 2019). The rich, diverse nature of this well-recorded sequence presents a great opportunity for the study of stress drops.

METHODS

Time-domain measurement of the spectrum

Isolating contributions from the earthquake source from contributions of the site and path to the seismogram continues to be a challenging problem for the field (Bindi *et al.*, 2023; Abercrombie *et al.*, 2024; Shearer *et al.*, 2024). Measurement of peak amplitudes in the time domain on narrowband-filtered displacement seismograms has several advantages for addressing this problem. Chief among them is the construction of the frequency-dependent attenuation function that describes the evolution of spectral amplitude with distance. This function is constructed empirically from the data, without the need to make assumptions about either geometric spreading or quality factor, Q. After correction for attenuation, the measurement of the peak amplitude is unique and can be targeted to a specific arrival. Here, we measure pre-event noise, and the P- and S-wave arrivals. By employing zero-phase time-domain filters, the peak values stay correctly localized in time on the seismogram, facilitating the measurement of both very low as well as very high frequencies. Filtering in the time domain also avoids problems associated with selection of windows and tapers for measurement in the spectral domain (Kay and Marple, 1981; Prieto *et al.*, 2007). Consequently, the method can be easily implemented in an automatic processing pipeline.

Measurement of the spectrum in the time domain from narrowband maximum amplitudes was introduced by Aki and

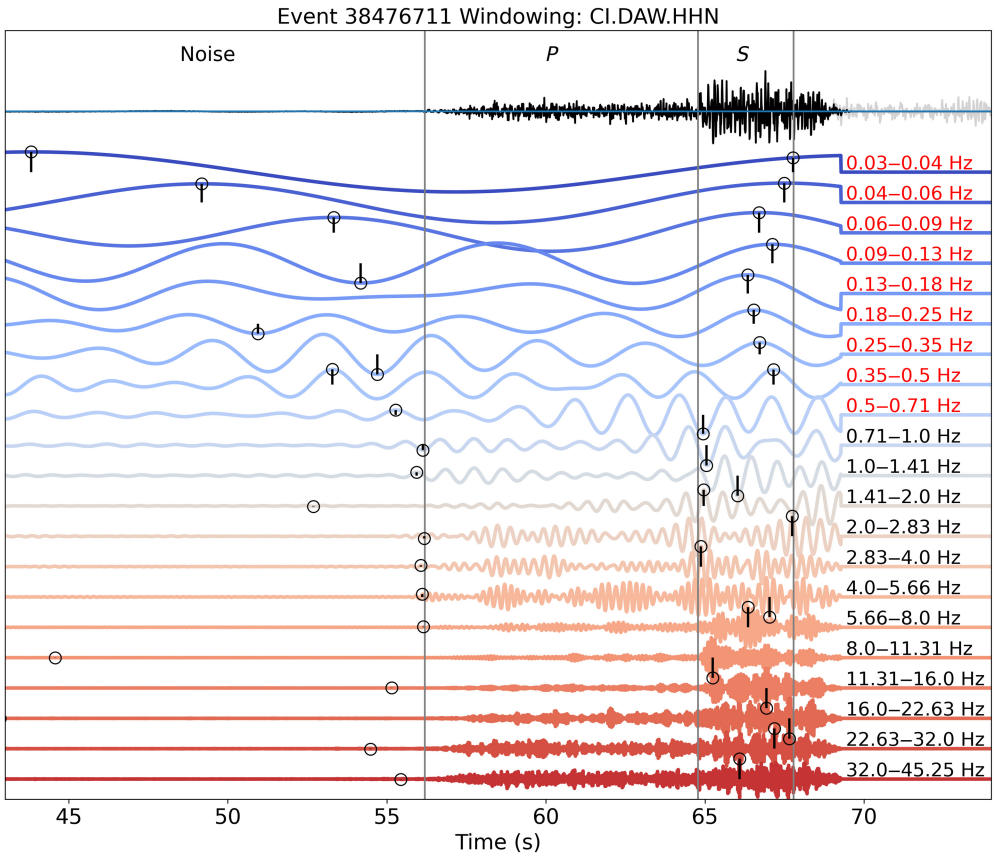

Figure 2. A filtered seismogram by our 21 band-passed filters with the noise, *P*-, and *S*-wave windows. Station CI.DAW is 68 km from event "38476711" (black star in Fig. 1), which has an M_w of 3.18, depth of 9.97 km, and an origin time of 7 July 2019 (14:28:18 UTC). Traces are normalized by their maximum amplitude for viewing. Maximum amplitude locations are shown for noise and *S*-wave windows with circles. The lower-frequency filter bands labeled in red have insufficient signal-to-noise ratio (SNR) for this seismogram and are excluded from further analysis. Colors correspond to these frequency bands for later figures. The color version of this figure is available only in the electronic edition.

Chouet (1975). A boxcar function $y(f)$ with constant amplitude C between angular frequencies ω_1 and ω_2, has an inverse Fourier transform given by

$$y(t) = \frac{1}{2\pi}\int_{|\omega_1|}^{|\omega_2|} Ce^{i\omega t}d\omega = 2C[f_1\mathrm{sinc}(\omega t) - f_2\mathrm{sinc}(\omega t)], \quad (3)$$

in which the relationship between angular frequency ω and frequency f is $\omega = 2\pi f$.

The maximum of this function occurs at $t = 0$, which simplifies the right side to $2C\Delta f$. Thus, the spectral amplitude of the box car is given by

$$C = \frac{\max(y(t))}{2\Delta f}. \quad (4)$$

We reconstruct the spectrum by band-passing a displacement seismogram through a set of filters. We use a set of 21 acausal half-octave Butterworth filters with two poles, ranging between frequencies 0.031 and 46 Hz. Frequency ranges for the filters are shown in Figure 2.

To prepare the seismogram for processing, we window it into noise, *P*, and *S* waves using the automatically determined phase picks provided with the data set (Fig. 2). The *P*-wave window is defined from 1 s before the *P*-wave arrival to 0.5 s before the *S*-wave arrival. The *S*-wave window is defined as from 0.5 s before the *S*-wave arrival to 3 s after. The noise window is defined by the section before the *P*-wave arrival of twice the length of the combined *P* and *S* windows.

To eliminate the effect of surface waves or trailing events, we applied a cosine taper to the seismogram at the end of the *S*-wave window. This prevents long-period energy from surface waves or larger trailing events from contaminating the *S*-window amplitudes, because we are using zero-phase filters (using causal filters just shifts the needed window length and has no perceptible benefit).

Preprocessing steps include removing the mean, high-pass filtering above 0.002 Hz, applying a 5% cosine taper, and removing the instrument response to displacement. Next, we apply the band-pass filters to the seismogram and measure the maximum of the absolute value of the amplitude in each of the windows (see Fig. 2). These amplitudes are corrected according to equation (4).

We employ this protocol on both horizontal components of the seismogram and measure the combined spectrum using the square root of the sum of the squares. An example of the measurements made with this method is shown in Figure 3, in which each colored line represents the combined horizontal spectrum of the *S* wave for a given station.

Path and site evaluation

To use equation (2) to solve for the path and site corrections in each frequency band, we make a few additions. We solve for the average regional attenuation as a function of distance for all stations and a site term at each station by modifying equation (2) to

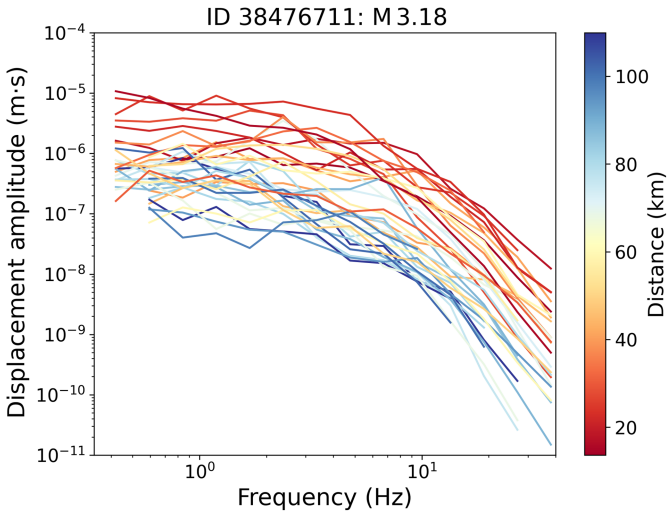

Figure 3. Observed displacement spectra for a single earthquake. Each line corresponds to a different station, colored by distance from the event. More distant stations, shown in blue, have lower amplitudes than nearer ones. Frequencies that do not meet the SNR threshold of four are omitted. The color version of this figure is available only in the electronic edition.

$$\log_{10}A_j(r,\gamma) = a_i \log_{10}A_0(r_i) + a_{i+1}\log_{10}A_0(r_{i+1}) + b_j M_{Lj} + c_\gamma S_\gamma, \quad (5)$$

in which j corresponds to the event, γ corresponds to the station, r corresponds to the event–station distance, and S is a station correction term. The coefficients a_i and a_{i+1} parameterize the distance dependence using nodes spaced at 10 km intervals. $b_j = 1$ and $c_\gamma = 1$ for events j and station γ, respectively, and are zero otherwise. We linearly interpolate between nodes to get each a ($a_i = 1 - a_{i+1} = \frac{r_{i+j}-r}{r_{i+j}-r_i}$). As such, i corresponds to the largest node such that $r_i < r$.

We solve for the site and path terms using equation (5) in a similar way to Andrews (1986) and Castro *et al.* (1990). Following Al-Ismail *et al.* (2023), we encode equation (5) into matrix form such that $d = Gm$, in which d is the data vector of amplitudes $A_j(r,\gamma)$ and m is a vector containing the $A_0(r_i)$, M_{Lj}, and S_γ terms. For the data, we use 719 events between magnitudes 3.3 and 3.7 to limit variability in corner frequency. To calibrate M_L through equation (5), we also assign 18 events with SCEDC preferred magnitudes between M 3.3 and 3.7 as calibration events. We append these magnitudes to the data vector and set $a_i = a_{i+1} = c_\gamma = 0$; $b_j = 1$ for these cases. We also require that the sum of the site terms is zero: $\sum_\gamma S_\gamma = 0$.

Finally, as in Al-Ismail *et al.* (2023), we apply a smoothing parameter λ and find the model that minimizes,

$$||d - Gm||_2^2 + \lambda||m||_2^2. \quad (6)$$

We use cross validation to determine the optimum value of $\lambda = 10$.

The path and site effects have strong frequency dependence. To account for this, we solve equation (6) for each of the 21 filter bands. Using the same procedure of band-pass filtering each seismogram, taking the maximum displacement amplitude in noise, P, and S windows, and normalizing by the bandwidth, we construct a data vector for each frequency range in Figure 2, and ensure data quality by only considering measurements with an SNR above four.

To connect the curves for the independently derived frequency bands and tie them to a physical scale, we normalize each of the curves to 10 km, and apply a frequency-dependent correction term to account for attenuation in the first 10 km of propagation using

$$A(f) = A_0(f)e^{\frac{-\pi r f}{\beta Q}}, \quad (7)$$

in which A_0 is the original amplitude, r is the event–station distance, β is the shear wavespeed, and Q is the quality factor. We set r to 10 km, β to 3.5 km/s, and Q to 100. Our choice of Q roughly aligns with measurements of the S-wave quality factor, Q_S, in the Ridgecrest area from Eberhart-Phillips (2016) for a shallow depth of 1 km.

To model the $1/r$ decay of body waves more accurately, we assign a functional form of the attenuation for distances less than 10 km,

$$A(r < 10\text{ km},f) = \frac{r}{r_{\text{norm}}}e^{\frac{-\pi r f}{\beta Q}}, \quad (8)$$

in which $r_{\text{norm}} = 10$ km is the normalization distance we chose earlier.

The path and site corrections are shown in Figures 4 and 5, respectively. In general, the higher frequencies have greater attenuation and differences become more pronounced as the frequency band increases. However, Q increases approximately with $\sqrt{f}$, as shown in Al-Ismail *et al.* (2023), which is similar to $f^{0.45}$ found by Raoof *et al.* (1999) and somewhat faster than found by Jordan (2024), who found that it increases as $f^{0.30}$ and $f^{0.37}$ for P and S waves, respectively. Note that the lowest five frequency bins were unstable due to low SNR. To remedy this, we set the station corrections above 3 log units for these frequencies to zero and the attenuation curves to equal the next stable frequency. For station corrections, we see that certain stations have systematic deviations from the other stations as a function of all frequencies. For example, the "PB" network shows low amplitudes across all frequencies compared to its counterparts. Both attenuation and station correction data can be found in Tables S1 and S2, available in the supplemental material to this article, respectively.

Fitting the model

We correct the observed displacement spectra in equation (1) by adding the frequency-dependent path and site corrections. The uncorrected spectra for the event shown in Figure 3

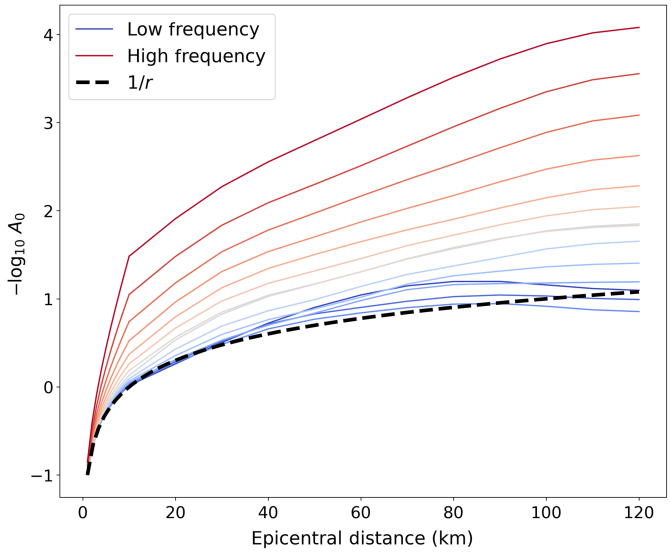

Figure 4. Amplitude decay curves as a function of distance and frequency after normalization to 10 km and frequency correction terms are applied. Note that all curves exceed the elastic geometrical spreading rate corresponding to the dashed line, "$1/r$" term. Values below 10 km showed $1/r$ spreading before the frequency-dependent correction. Colors match the frequency ranges shown in Figure 2. Values of the curves can be found in Table S1. The color version of this figure is available only in the electronic edition.

display clear distance dependencies, with more distant stations having lower amplitudes at all frequencies compared with closer stations. After correction in Figure 6, all curves move closer together. We summarize the event spectrum using the median value in each frequency band. Note that when taking the median, we only use data with SNR above four with at least three stations contributing to a given frequency bin.

We fit an ω^2 Brune model to the median spectrum (Brune, 1970),

$$u(f) = \frac{\Omega_0}{(1 + \frac{f}{f_c})^2}, \tag{9}$$

in which $u(f)$ is the source displacement spectrum, Ω_0 is the low-frequency asymptote, and f_c is the corner frequency.

We use a nonlinear least-squares solver in Python (curve_fit from scipy) to fit the functional form of the Brune model in logarithmic space. Because we are not using individual spectral ordinates, but rather average values in each half-octave band, we need to integrate the result of the Brune model across the half-octave frequency bands, as done in Al-Ismail *et al.* (2023), when we compare the model prediction to data. A Brune model fit, using the time-domain method, to an idealized noisy spectrum can be found in Figure S1.

Results from the fitting yield optimal low-frequency limits (Ω_0) and corner frequencies (f_c). We estimate uncertainties of these values with a bootstrapping approach by taking 100 different populations of spectra for each event. Within each population we choose random spectra with replacement until the original number of stations for that event is reached. At this point, the 95% confidence intervals are determined for the corner frequency and moments. We propagate uncertainties with the uncertainties library in Python (Lebigot, 2023). In Figure 7, we also consider the trade-off between fitting of f_c and Ω_0. We plot lines of constant misfit as contours and show a similar negative correlation, as discussed in Yoshimitsu *et al.* (2019) and Al-Ismail *et al.* (2023).

To convert our low-frequency limits to moment, we use the proportionality between Ω_0 and M_0 as in Aki and Richards (2002),

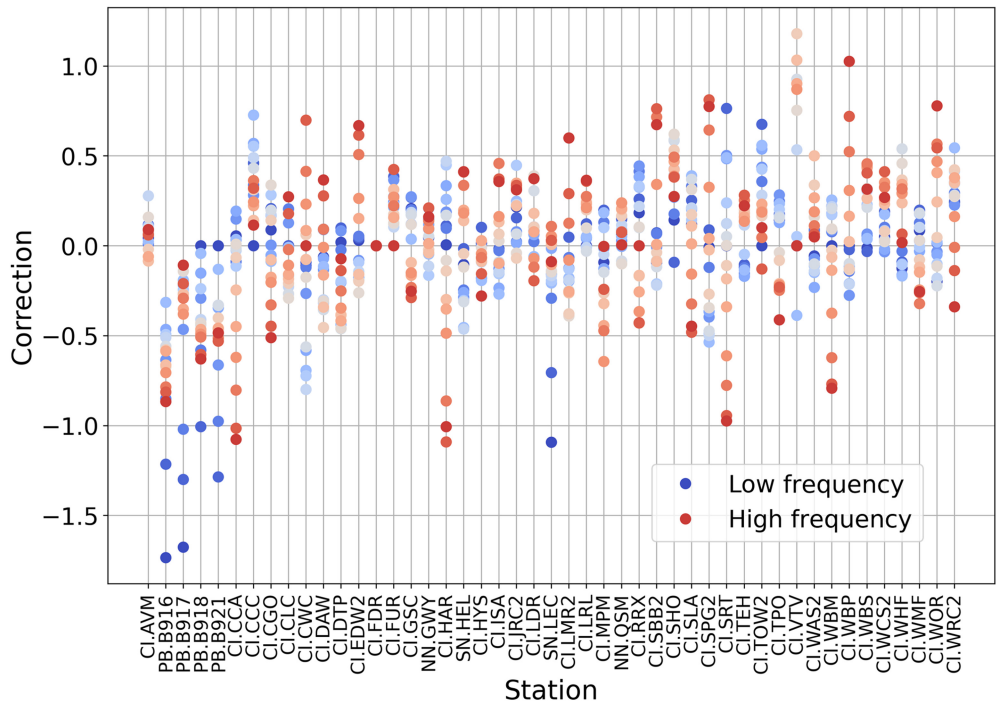

Figure 5. Station correction terms in log space as a function of frequency. These corrections, which were subtracted from the observed spectra, represent the relative amplitude difference for different sites recording an event at the same distance. The red and blue points correspond to higher- and lower-frequency corrections, respectively. Colors match the frequency ranges shown in Figure 2. Corrections can be found in Table S2. The color version of this figure is available only in the electronic edition.

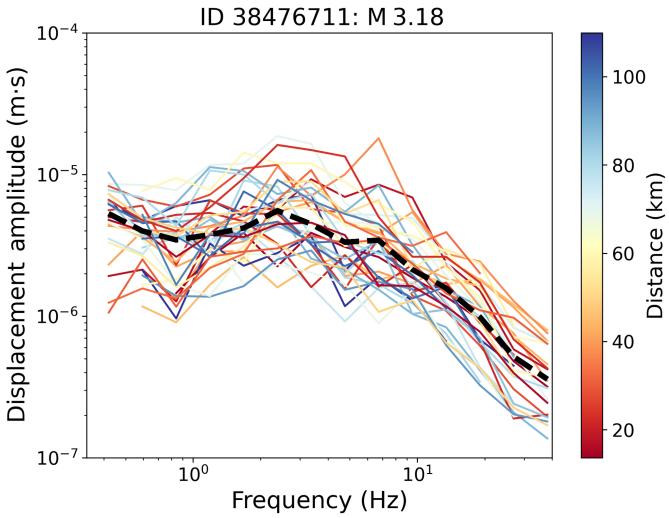

Figure 6. Corrected displacement spectra for the event shown in Figure 3. Note that differences in amplitude with distance are no longer apparent. Median shown in black-dashed line. The color version of this figure is available only in the electronic edition.

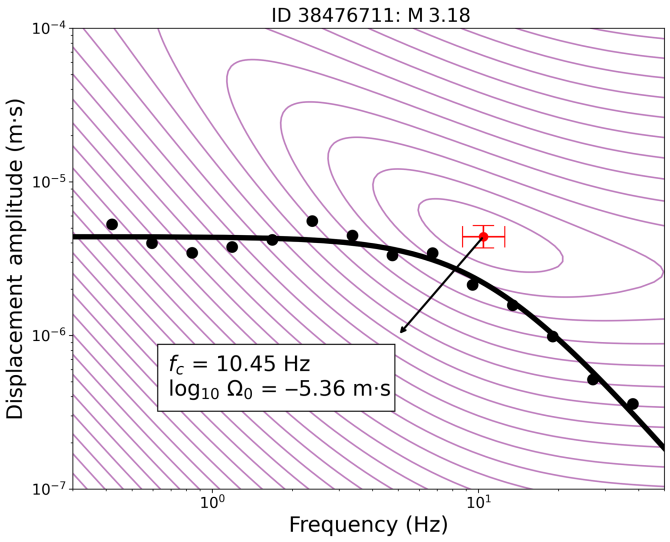

Figure 7. Brune model fit of the median corrected displacement spectrum for event "38476711." The black dots are the median of the corrected spectral amplitudes, and the black line is the Brune fit, with moment and corner frequency given by the values shown with the red dot. Contours show levels of constant misfit, and error bars are determined from bootstrapping. The color version of this figure is available only in the electronic edition.

$$\Omega_0 = 2\frac{M_0\phi}{4\pi\rho\beta^3 r}, \tag{10}$$

in which ϕ is the average of the *S*-wave radiation pattern over the focal sphere, ρ is the density, β is the shear wavespeed, and r is the distance corresponding to a $1/r$ geometrical spreading factor. The factor of 2 comes from the free-surface amplification. To find the proportionality, we assume that $\phi = 0.63$, $\rho = 2700$ kg/m^3, $\beta = 3.5$ km/s, and $r = 10$ km following our normalization distance from before. This gives us the following constant of proportionality:

$$M_0 = (1.15 \times 10^{19})\Omega_0. \tag{11}$$

We enforce a quality control criterion on the data to have a normalized rms misfit from the idealized Brune model in log space of less than 0.2 units. Events that have a larger trailing event within 20 s are not considered due to the possibility of contamination of the window, and we require a minimum of eight stations to contribute to the spectrum. The minimum station criteria ensure accurate averaging over the radiation pattern azimuth. We also removed events exceeding an uncertainty of 0.5 in magnitude or 20 Hz in corner frequency. These events primarily correspond to data that were either entirely above or below the corner, respectively. These quality control measures reduced the number of events to 5707 of the original 13,000 events.

RESULTS

We calculate moments according to equation (11) and convert them to Moment magnitude, M_w, via the relation by Hanks and Kanamori (1979):

$$M_w = \frac{2}{3}\log_{10}(M_0) - 6.07. \tag{12}$$

Comparisons of fit moment magnitudes are plotted against the catalog magnitudes provided by SCEDC (Fig. 8). The color bar shows how many stations were used to compute the median for each event. We find that moment and corner-frequency uncertainties are lower for events with more station measurements. Magnitudes agree well with catalog magnitudes above M 3.5. The catalog generally reports M_w above M 3.5 and M_L below M 3.5. This scaling below M 3.5 is consistent with a deviation of M_L from M_w (Deichmann, 2017). We find that below a catalog magnitude of 3.5, our moments scale with M_L as: $M_w = 0.71M_L + 1.01$. This resembles the relationship of $M_w = 0.0376M_L^2 + 0.646M_L + 0.814$ by Tan *et al.* (2021), which was calibrated for central Italy, more closely than initial results by Al-Ismail *et al.* (2023) (see Fig. S2).

Figure 9 shows our corner frequencies plotted against moment for the quality-controlled set of earthquakes. We calculate the stress drop $\Delta\sigma$ from these two quantities according to the relationship of Eshelby (1957),

$$\Delta\sigma = \frac{7M_0}{16}\frac{f_c^3}{(k\beta)^3}, \tag{13}$$

with $\beta = 3.5$ km/s and in which k is a constant depending on the source model, which we assume is 0.37 for *S* waves (Brune, 1970; Hanks and Thatcher, 1972). We find a median stress drop of 1.65 MPa. Although stress drops are variable, we find little evidence for scaling with seismic moment for events

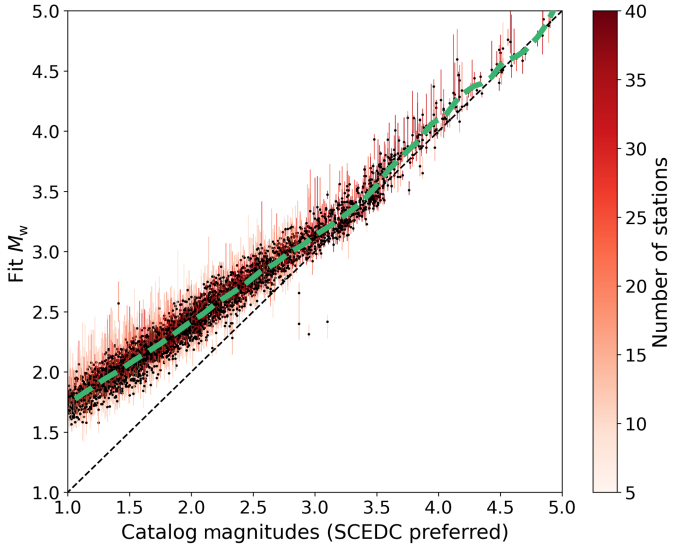

Figure 8. Moment magnitudes from our spectral fitting approach versus the Southern California Earthquake Data Center (SCEDC) preferred magnitudes. The green line represents the moving median. The catalog magnitudes generally report M_w above M 3.5 and M_L below. The dashed line is the one-to-one line. Error bars represent the 95% confidence intervals determined by bootstrapping. The color bar indicates how many stations were used to make up the median. The color version of this figure is available only in the electronic edition.

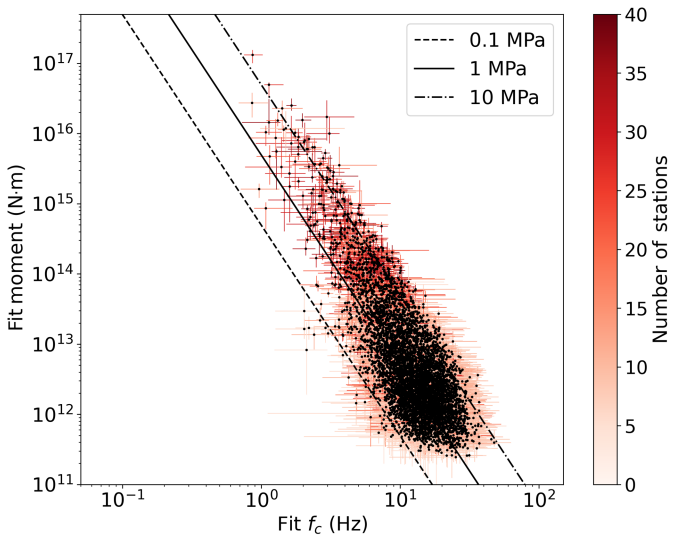

Figure 9. Corner frequencies plotted against moment. Constant stress-drop scaling is shown with dashed lines. Error bars represent the 95% confidence intervals determined by bootstrapping. The color bar indicates how many stations were used to determine the median. A visualization of the kernel density of the population can be found in Figure S3. The color version of this figure is available only in the electronic edition.

larger than 10^{14} N · m. For smaller events, stress drops are smaller and scaling is more apparent.

As seen in Figure 10, these low stress drops are strongly grouped by region. As found in Trugman (2020), the northern

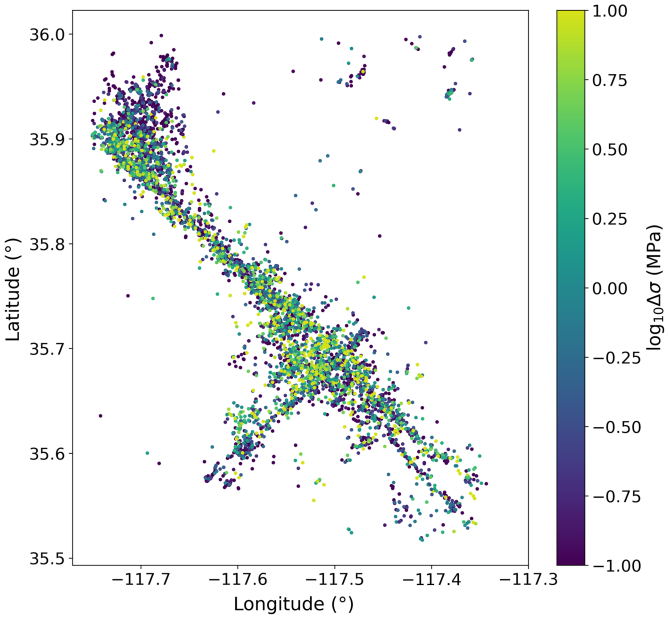

Figure 10. Stress drop plotted in space. Events with higher stress drops are preferentially plotted on top for illustration purposes. A plot of these stress drops in 3D space can be found in Figure S4. The color version of this figure is available only in the electronic edition.

portion of the sequence appears to have lower stress-drop values, whereas the main body surrounding the mainshock appears to have higher than average stress drops. Lower stress drops are also seen at the terminal ends of the mainshock rupture and the perpendicular 4 July M_w 6.4 foreshock.

STRESS-DROP VARIABILITY WITH DEPTH, TIME, AND MAGNITUDE

The notion of self-similarity, or constant stress drop with magnitude, has been a subject of extensive research and debate for decades (Aki, 1972). Constant stress drop suggests similar source physics across different magnitude ranges and different tectonic environments. Although some studies report a deviation from self-similarity (Mayeda and Walter, 1996; Mayeda *et al.*, 2007), others find a consistent measurement across many orders of magnitude (Abercrombie, 1995; Ide and Beroza, 2001; Allmann and Shearer, 2009; Baltay *et al.*, 2013; Yoshimitsu *et al.*, 2014).

In this study, we find that stress drop increases both with depth and with magnitude. As shown in Figure 11, stress drop as a function of magnitude and binned by two depth ranges reveals strong correlations with both. The two populations are distinct, with events between 7 and 10 km depth having ~4 times the stress drop of events between 1 and 4 across magnitudes. Stress drop also increases by approximately a factor of 4 between M_w 2 and 3 and a factor of 2 between M_w 3 and 4. Because of the inverse cubic dependence of stress drop on f_c, this corresponds to a 60% decrease of f_c for the deeper events

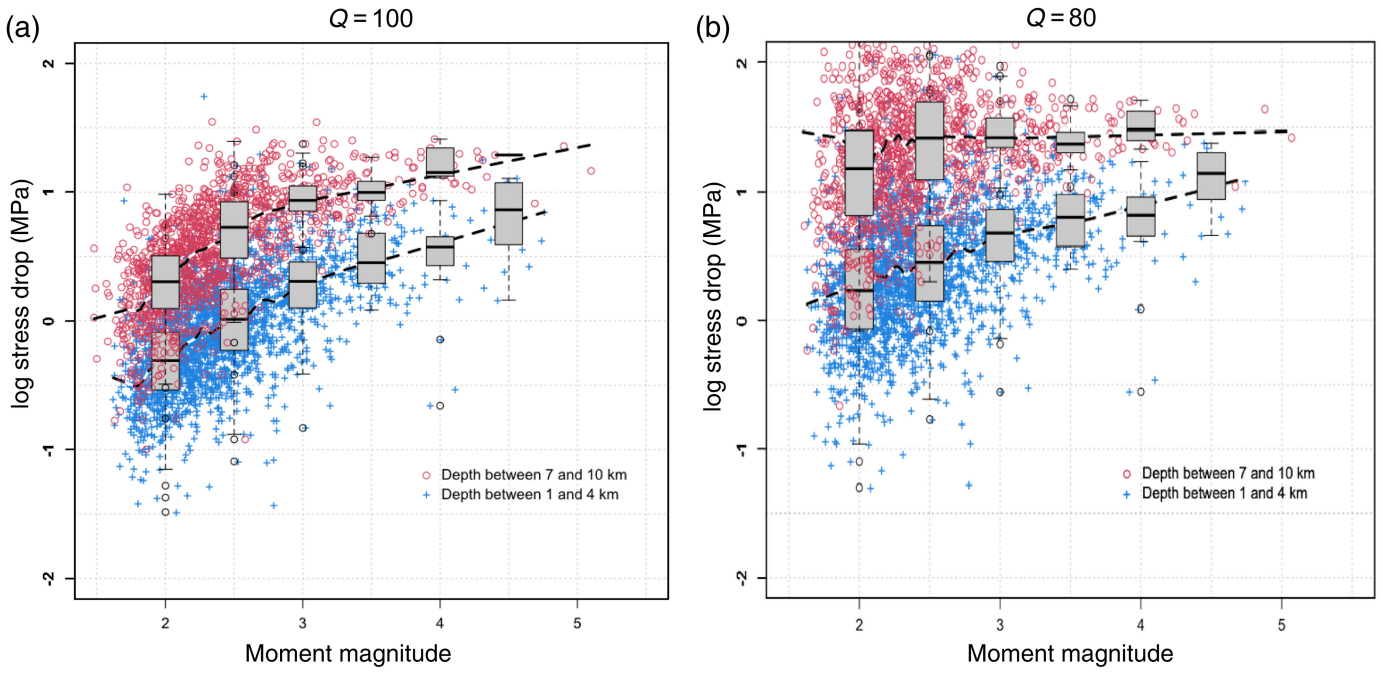

Figure 11. Stress drop as a function of moment magnitude with (a) Q = 100 and (b) Q = 80, for two populations of events. Earthquakes with depths between 1 and 4 km are plotted in blue and earthquakes with depths between 7 and 10 km are plotted in red. The dashed lines are the smoothed estimate of the running median, and box plots show inner quartile ranges. The black circles are outliers. The color version of this figure is available only in the electronic edition.

compared to the shallower ones. These systematics might be due to the simplified assumptions about the Earth model used to compute seismic moment and stress drop, including a constant velocity everywhere and a frequency-independent Q = 100 in the first 10 km of the attenuation function.

We also observe an increase in stress drop in the immediate aftermath of the mainshocks (Fig. 12a). Although this trend is apparent, it is important to note that our quality control removed events with 20 s interarrival times between larger, trailing events. This has the effect of removing smaller-magnitude events in the busiest parts of the sequence, shown by the gap under the primary peak. Although the median stress drop possibly increased with time following the mainshock, this effect may be exaggerated by our event selection criteria. Inclusion of all events regardless of data quality lowers the peak median stress drop in Figure 12b from 6.2 to 5.8 MPa (see Fig. S5), so that a gap persists below the peak.

As noted earlier, a possible explanation for our apparent magnitude scaling could come from the method used to connect the 21 narrowband attenuation curves. We chose to use a value of Q = 100 at 10 km to tie the frequency-dependent attenuation relations together. Although consistent with independent evidence (Eberhart-Phillips, 2016), this is likely an oversimplified model for how amplitudes decay at short distances. A lower value for Q in the first 10 km would put more high-frequency energy back into the spectrum and increase the measured corner frequency. The effect is relatively minor for events M >3, but significant for those M <3, as the higher the corner frequency, the greater the attenuation at fixed distance. A lower Q value would move smaller-magnitude events with (on average) higher corner frequencies toward higher stress drops, reducing the break from self-similarity. By reducing the path averaged Q from 100 to 80 in the first 10 km, the scaling for the 7–10-km-deep events was removed, and it was reduced for the 1–4-km-deep events. This change also increased the average stress drop by a factor of 3–4, higher than the more typically determined range of ∼3–20 MPa (Abercrombie *et al.*, 2024).

We also considered the effect of replacing the assumed β = 3.5 km/s with a more accurate representation of the velocities. Changing β affects seismic moment and source dimension, both of which appear in the Eshelby formula for stress drop (equation 13). Under the assumptions of equation (10) to obtain seismic moment, the two effects cancel, and there is no change in stress drop when varying source velocity. A surprising result to us. If we had instead used the formula for seismic moment that includes both source and receiver velocity and density (Aki and Richards, 2002), then the stress drop would change as the source velocity varies. In this case, the change in stress drop scales as $(V_{\text{actual}}/V_{\text{assumed}})^{-1/2}$, rather weak scaling.

Although the stress drops themselves are not strongly adjusted by changes in velocity at the source, moment magnitude will be adjusted by a factor of $5/3\log(V_{\text{new}}/V_{\text{old}})$ by 0.05, which are shown in Figure S2.

A further source of the apparent non-self-similarity could be found in assumptions about the behavior of the spectrum

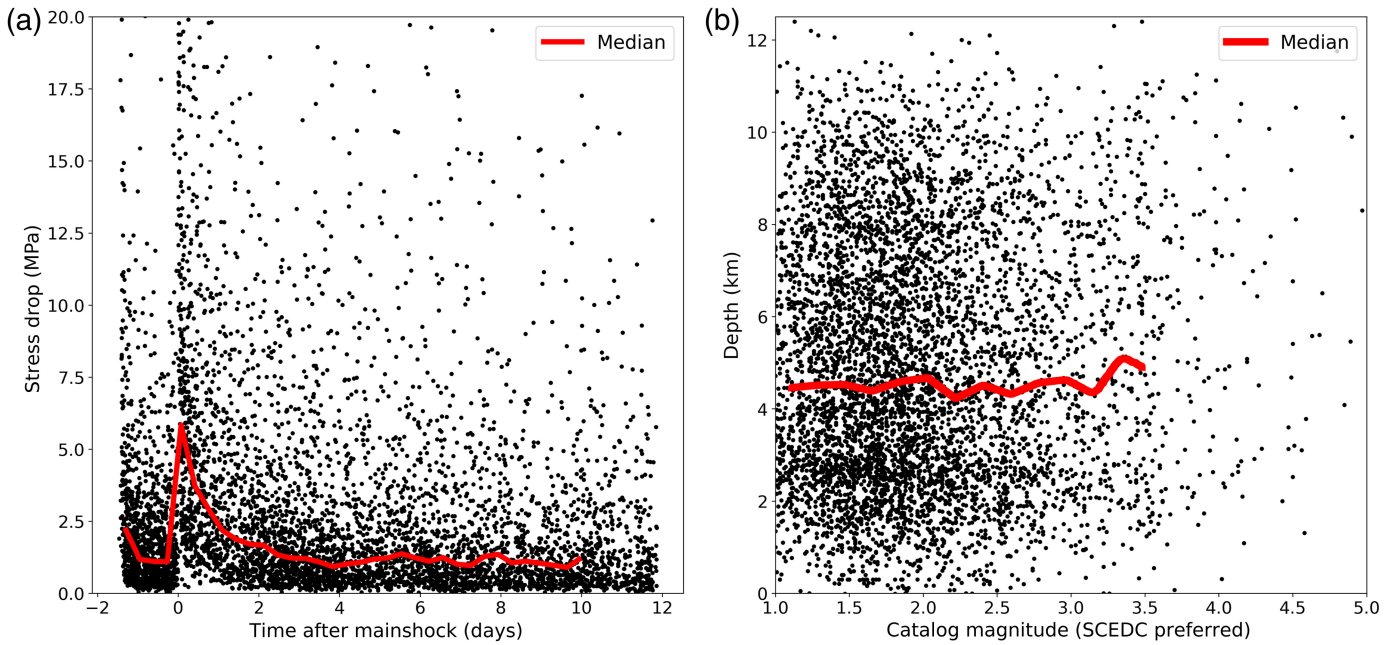

Figure 12. Trends in the results. (a) Stress drop plotted as a function of time. The moving median is plotted in red for both figures. (b) Depth versus catalog magnitude. There is no obvious trend between the two. The color version of this figure is available only in the electronic edition.

past the corner frequency. A change in fall-off rate could correct the increase of stress drop with magnitude (Trugman and Shearer, 2017; Trugman, 2020), because corner frequency tends to increase with steeper fall-off rates. Because fitting and changes in corner frequencies are done in the log domain, an equivalent increase in corner frequency at higher frequencies (smaller events) due to an increase in the fall-off would tend to shift stress drops more than at lower frequencies. Unmodeled deviations from a simple circular source, including the presence of strong source radiation heterogeneity and directivity, which could contribute to the apparent scaling. As mentioned in Trugman (2020), the immaturity of the fault system could introduce more rupture complexity than a more mature fault system. However, variations in fall-off rate are challenging to recover due to additional trade-offs between fall-off rate, corner frequency, attenuation, and moment.

Finally, it is worth noting that because we removed events with excessively high corner frequency uncertainty, a bias in our measurements could be introduced by removing events with corners close to the upper-frequency limit of the data. These events would tend to have higher stress drops than others and thus, their omission could bias the population. Relaxing the quality control criterion of the uncertainty threshold of the corner frequency results in 1017 extra events. However, these events do not significantly change the observed magnitude and depth trends in the data. Therefore, we do not believe that this quality control measure is a significant contributor to the observed relationships between stress drop with depth and magnitude.

The observation of increasing stress drop with depth (Fig. 11) is apparent at all magnitudes. There is at most a weak correlation between depth and magnitude (Fig. 12b), which cannot adequately account for the observed trend. Recent studies have shown a reduction of depth scaling using depth-dependent EGF terms (Abercrombie *et al.*, 2021). Spectral-ratio EGF methods, in particular, provide insight into both depth and magnitude scaling because their cancellation of path contributions requires fewer assumptions than modeling path and site features individually (Ide *et al.*, 2003; Abercrombie *et al.*, 2021).

Our attenuation model does not account for depth, so it is reasonable to ask whether a more complex model would correct the depth dependence of stress drop. We have experimented with computing separate attenuation relations for events at depths less than 6 km and events deeper than 6 km. The result shows a modest reduction in the depth scaling, but not nearly enough to remove it. It is possible that this is because there is another trade-off with distance: waves from shallow events observed at large epicentral distance will still sample greater depths. A more complex attenuation model that accounts for the ray path in a depth-dependent Q model would be useful to explore in future work. We also note that Bindi *et al.* (2021) consider more depth complexity in their attenuation model by explicitly incorporating both the epicentral distance and hypocentral depth, and found it did not remove the scaling effect for this same sequence.

It is possible that the scaling relationships we observe are not artifacts but rather represent a true break from constant stress-drop scaling, with stress drop increasing with both magnitude and depth. Mayeda *et al.* (2007) suggest that the rerupturing of fault in aftershocks involves different dynamics than for foreshock and mainshock rupture. This explanation would be consistent with the magnitude and time dependencies of

stress drop in this study. However, caution due to the earlier reasons should be taken with this interpretation. Instead, systematic trends within other studies of Abercrombie *et al.* (2024) should be analyzed for potential trends and assumptions underlying those results.

CONCLUSION

We measure the seismic spectrum of 5707 events in the 2019 Ridgecrest sequence from maximum amplitudes expressed in the time domain. Using a similar workflow to that of Richter in the development of the local magnitude scale, we solve for frequency-dependent path and site terms to correct our spectra to the source. We fit an omega-squared Brune model to these spectra and find reliable moment magnitudes and uncertainties for events as small as M_L 1.0. We find a strong stress-drop scaling with both depth and magnitude. Possible explanations for such scaling could arise in assumptions about the source or path, and further investigation and comparisons with other studies are important for resolution of such possibilities.

DATA AND RESOURCES

The data used in this study come from the publicly available data set from the Southern California Earthquake Data Center (Southern California Earthquake Center [SCEC], 2013). Specifically, a subset of the data set of over 12,000 relocated events from Trugman (2020) in the two-week period between 4 and 17 July 2019 following the M 7.1 mainshock. The supplemental material contains additional plots showing proof of concept of the method and tables of attenuation and site corrections. Specifically, Figure S1 compares the maximum amplitude method for a test case with a ground-truth moment and corner frequency. Figure S2 shows the best-fit line through the M_w versus M_L plot below M_L 3.5 for constant and depth-dependent velocity models and compares our estimates to that of Tan *et al.* (2021). Figure S3 shows the kernel density estimation for the moment versus corner-frequency plot for a better understanding of the population. Figure S4 shows the 3D distribution of stress drops in space. Figure S5 shows the stress drop versus time for all events in the data set that had discernable stress drops. Table S1 contains the amplitude decay corrections ($-\log_{10} A_0$) as a function of frequency and distance. Table S2 contains the station corrections as a function of station and frequency. Table S3 contains source parameter results for three different models discussed. Notably, corner frequency, moment, and stress drop are reported for each.

DECLARATION OF COMPETING INTERESTS

The authors acknowledge that there are no conflicts of interest recorded.

ACKNOWLEDGMENTS

The authors thank Dino Bindi, Junghyun Park, and anonymous reviewers for helpful feedback. This research was supported by the Statewide California Earthquake Center (Contribution Number 14086). Southern California Earthquake Center (SCEC) is funded by National Science Foundation (NSF) Cooperative Agreement EAR-2225216 and U.S. Geological Survey (USGS) Cooperative Agreement G24AC00072-00.

REFERENCES

Abercrombie, R. E. (1995). Earthquake source scaling relationships from -1 to 5 ml using seismograms recorded at 2.5-km depth, *J. Geophys. Res.* **100,** no. B12, 24,015–24,036.

Abercrombie, R. E. (2021). Resolution and uncertainties in estimates of earthquake stress drop and energy release, *Phil. Trans. Roy. Soc. Lond. A* **379,** no. 2196, 20200131, doi: 10.1098/rsta.2020.0131.

Abercrombie, R. E., A. S. Baltay, S. Chu, T. Taira, D. Bindi, O. S. Boyd, X. Chen, E. S. Cochran, E. G. Devin, D. S. Dreger, *et al.* (2024). Overview of the SCEC/USGS community stress drop validation study using the 2019 Ridgecrest earthquake sequence, *Bull. Seismol. Soc. Am.* (in revision).

Abercrombie, R. E., D. T. Trugman, P. M. Shearer, X. Chen, J. Zhang, C. N. Pennington, J. L. Hardebeck, T. H. Goebel, and C. J. Ruhl (2021). Does earthquake stress drop increase with depth in the crust? *J. Geophys. Res.* **126,** no. 10, e2021JB022314, doi: 10.1029/2021JB022314.

Aki, K. (1972). Earthquake mechanism, *Tectonophysics* **13,** nos. 1/4, 423–446.

Aki, K., and B. Chouet (1975). Origin of coda waves: Source, attenuation, and scattering effects, *J. Geophys. Res.* **80,** no. 23, 3322–3342.

Aki, K., and P. G. Richards (2002). *Quantitative Seismology*, University Science Books, Sausalito, California.

Al-Ismail, F., W. L. Ellsworth, and G. C. Beroza (2023). A time-domain approach for accurate spectral source estimation with application to Ridgecrest, California, earthquakes, *Bull. Seismol. Soc. Am.* **113,** no. 3, 1091–1101.

Allmann, B. P., and P. M. Shearer (2009). Global variations of stress drop for moderate to large earthquakes, *J. Geophys. Res.* **114,** no. B1, doi: 10.1029/2008JB005821.

Andrews, D. (1986). Objective determination of source parameters and similarity of earthquakes of different size, in *Earthquake Source Mechanics*, S. Das, J. Boatwright, and C. H. Scholz (Editors), Vol. 37, American Geophysical Union, Washington, D.C., 259–267, doi: 10.1029/GM037p0259.

Baltay, A. S., T. C. Hanks, and G. C. Beroza (2013). Stable stress-drop measurements and their variability: Implications for ground-motion prediction, *Bull. Seismol. Soc. Am.* **103,** no. 1, 211–222.

Barnhart, W. D., G. P. Hayes, and R. D. Gold (2019). The July 2019 Ridgecrest, California, earthquake sequence: Kinematics of slip and stressing in cross-fault ruptures, *Geophys. Res. Lett.* **46,** no. 21, 11,859–11,867.

Bindi, D., H. N. Razafindrakoto, M. Picozzi, and A. Oth (2021). Stress drop derived from spectral analysis considering the hypocentral depth in the attenuation model: Application to the Ridgecrest region, California, *Bull. Seismol. Soc. Am.* **111,** no. 6, 3175–3188.

Bindi, D., D. Spallarossa, M. Picozzi, A. Oth, P. Morasca, and K. Mayeda (2023). The community stress-drop validation study—part II: Uncertainties of the source parameters and stress drop analysis, *Seismol. Res. Lett.* **94,** no. 4, 1992–2002.

Brune, J. N. (1970). Tectonic stress and the spectra of seismic shear waves from earthquakes, *J. Geophys. Res.* **75,** no. 26, 4997–5009.

Castro, R., J. Anderson, and S. Singh (1990). Site response, attenuation and source spectra of s waves along the Guerrero, Mexico, subduction zone, *Bull. Seismol. Soc. Am.* **80,** no. 6A, 1481–1503.

Chouet, B., K. Aki, and M. Tsujiura (1978). Regional variation of the scaling law of earthquake source spectra, *Bull. Seismol. Soc. Am.* **68,** no. 1, 49–79.

Deichmann, N. (2017). Theoretical basis for the observed break in ml/m w scaling between small and large earthquakes, *Bull. Seismol. Soc. Am.* **107,** no. 2, 505–520.

Eberhart-Phillips, D. (2016). Northern California seismic attenuation: 3D QP and QS models, *Bull. Seismol. Soc. Am.* **106,** no. 6, 2558–2573.

Eshelby, J. D. (1957). The determination of the elastic field of an ellipsoidal inclusion, and related problems, *Proc. Math. Phys. Sci.* **241,** no. 1226, 376–396.

Hanks, T. C., and H. Kanamori (1979). A moment magnitude scale, *J. Geophys. Res.* **84,** no. B5, 2348–2350.

Hanks, T. C., and W. Thatcher (1972). A graphical representation of seismic source parameters, *J. Geophys. Res.* **77,** no. 23, 4393–4405.

Ide, S., and G. C. Beroza (2001). Does apparent stress vary with earthquake size? *Geophys. Res. Lett.* **28,** no. 17, 3349–3352.

Ide, S., G. C. Beroza, S. G. Prejean, and W. L. Ellsworth (2003). Apparent break in earthquake scaling due to path and site effects on deep borehole recordings, *J. Geophys. Res.* **108,** no. B5, doi: 10.1029/2001JB001617.

Jordan, T. H. (2024). Crustal structure of southern California from velocity and attenuation tomography, *Ann. Geophys.* **67,** S429–S429.

Kay, S. M., and S. L. Marple (1981). Spectrum analysis—A modern perspective, *Proc. IEEE* **69,** no. 11, 1380–1419.

Lebigot, E. O. (2023). Uncertainties: A python package for calculations with uncertainties (Version 3.1.7), available at https://pythonhosted.org/uncertainties/ (last accessed June 2024).

Mayeda, K., and W. R. Walter (1996). Moment, energy, stress drop, and source spectra of western united states earthquakes from regional coda envelopes, *J. Geophys. Res.* **101,** no. B5, 11,195–11,208.

Mayeda, K., L. Malagnini, and W. R. Walter (2007). A new spectral ratio method using narrow band coda envelopes: Evidence for non-self-similarity in the hector mine sequence, *Geophys. Res. Lett.* **34,** no. 11, doi: 10.1029/2007GL030041.

Prieto, G., R. Parker, D. Thomson, F. Vernon, and R. Graham (2007). Reducing the bias of multitaper spectrum estimates, *Geophys. J. Int.* **171,** no. 3, 1269–1281.

Raoof, M., R. Herrmann, and L. Malagnini (1999). Attenuation and excitation of three-component ground motion in southern California, *Bull. Seismol. Soc. Am.* **89,** no. 4, 888–902.

Rautian, T., and V. Khalturin (1978). The use of the coda for determination of the earthquake source spectrum, *Bull. Seismol. Soc. Am.* **68,** no. 4, 923–948.

Rautian, T., V. Khalturin, V. Martynov, and P. Molnar (1978). Preliminary analysis of the spectral content of p and s waves from local earthquakes in the Garm, Tadjikistan region, *Bull. Seismol. Soc. Am.* **68,** no. 4, 949–971.

Richter, C. F. (1935). An instrumental earthquake magnitude scale, *Bull. Seismol. Soc. Am.* **25,** no. 1, 1–32.

Ross, Z.E., B. Idini, Z. Jia, O.L. Stephenson, M. Zhong, X. Wang, Z. Zhan, M. Simons, E.J. Fielding, S.H. Yun, *et al.* (2019). Hierarchical interlocked orthogonal faulting in the 2019 Ridgecrest earthquake sequence, *Science* **366,** no. 6463, 346–351.

Shearer, P. M., I. Vandevert, W. Fan, R. E. Abercrombie, D. Bindi, G. Calderoni, X. Chen, W. L. Ellsworth, R. M. Harrington, Y. Huang, *et al.* (2024). Earthquake source spectra estimates vary widely for two Ridgecrest aftershocks because of differences in attenuation corrections, *Bull. Seismol. Soc. Am.* doi: 10.1785/0120240134.

Shelly, D. R. (2020). A high-resolution seismic catalog for the initial 2019 Ridgecrest earthquake sequence: Foreshocks, aftershocks, and faulting complexity, *Seismol. Res. Lett.* **91,** no. 4, 1971–1978.

Southern California Earthquake Center (SCEC) (2013). Southern California Earthquake Center, *Caltech*, Dataset, doi: 10.7909/C3WD3xH1.

Tan, Y.J., F. Waldhauser, W.L. Ellsworth, M. Zhang, W. Zhu, M. Michele, L. Chiaraluce, G.C. Beroza, and M. Segou (2021). Machine-learning-based high-resolution earthquake catalog reveals how complex fault structures were activated during the 2016-2017 central Italy sequence, *Seism. Rec.* **1,** no. 1, 11–19.

Thatcher, W., and T. C. Hanks (1973). Source parameters of southern California earthquakes, *J. Geophys. Res.* **78,** no. 35, 8547–8576.

Trugman, D. T. (2020). Stress-drop and source scaling of the 2019 Ridgecrest, California, earthquake sequence, *Bull. Seismol. Soc. Am.* **110,** no. 4, 1859–1871.

Trugman, D. T., and P. M. Shearer (2017). Application of an improved spectral decomposition method to examine earthquake source scaling in southern California, *J. Geophys. Res.* **122,** no. 4, 2890–2910.

Tsujiura, M. (1973). Spectrum of seismic waves and its dependence on magnitude, *J. Phys. Earth* **21,** no. 4, 373–391.

Yoshimitsu, N., W. L. Ellsworth, and G. C. Beroza (2019). Robust stress drop estimates of potentially induced earthquakes in Oklahoma: Evaluation of empirical green's function, *J. Geophys. Res.* **124,** no. 6, 5854–5866.

Yoshimitsu, N., H. Kawakata, and N. Takahashi (2014). Magnitude- 7 level earthquakes: A new lower limit of self-similarity in seismic scaling relationships, *Geophys. Res. Lett.* **41,** no. 13, 4495–4502.

Manuscript received 15 August 2024
Published online 9 January 2025